



1 **Quantile Sampling: a robust and simplified pixel-based** 2 **multiple-point simulation approach**

3 Mathieu Gravey¹, Grégoire Mariethoz¹

4 ¹ University of Lausanne, Faculty of Geosciences and Environment, Institute of Earth Surface Dynamics,
5 Switzerland

6 *Correspondence to:* Mathieu Gravey (mathieu.gravey@unil.ch)

7 **Highlights**

- 8 • A new approach is proposed for pixel-based multiple-point geostatistics simulation.
- 9 • The method is flexible and straightforward to parametrize.
- 10 • It natively handles continuous and multivariate simulations.
- 11 • High computational performance with predictable simulation times.
- 12 • A free and open-source implementation is provided.

13 **Abstract**

14 Multiple-point geostatistics enable the realistic simulation of complex spatial structures by
15 inferring statistics from a training image. These methods are typically computationally
16 expensive and require complex algorithmic parametrizations. The approach that is presented in
17 this paper is easier to use than existing algorithms, as it requires few independent algorithmic
18 parameters. It is natively designed for handling continuous variables, and quickly implemented
19 by capitalizing on standard libraries. The algorithm can handle incomplete training images of
20 any dimensionality, with categorical or/and continuous variables, and stationarity is not
21 explicitly required. It is possible to perform unconditional or conditional simulations, even with
22 exhaustively informed covariates. The method provides new degrees of freedom by allowing
23 kernel weighting for pattern matching. Computationally, it is adapted to modern architectures
24 and runs in constant time. The approach is benchmarked against a state-of-the-art method. An
25 efficient open-source implementation of the algorithm is released and can be found here
26 (<https://github.com/GAIA-UNIL/G2S>), to promote reuse and further evolution.

27 **Keywords**

28 Multiple-point statistics, stochastic simulation, continuous variable, training image, cross-
29 correlation, Fourier transform.

30 **1. Introduction**

31 Geostatistics is widely used to generate stochastic random fields for modeling and
32 characterizing spatial phenomena such as Earth surface features and geological structures.
33 Commonly used methods, such as the sequential Gaussian simulation (Gómez-Hernández and
34 Journel, 1993) and turning bands algorithms (Matheron, 1973), are based on kriging (e.g.,
35 Graeler et al., 2016; Li and Heap, 2014; Tadić et al., 2017; 2015). This family of approaches
36 implies spatial relations using exclusively pairs of points and expresses these relations using



37 covariance functions. In the last two decades, multiple point statistics (MPS) emerged as a
38 method for representing more complex structures using high-order nonparametric statistics
39 (Guardiano and Srivastava, 1993). To do so, MPS algorithms rely on training images, which
40 are images with similar characteristics to the modeled area. Over the last decade, MPS has been
41 used for stochastic simulation of random fields in a variety of domains such as geological
42 modeling (e.g., Barfod et al., 2018; Strebelle et al., 2002), remote sensing data processing (e.g.,
43 Gravey et al., 2019; Yin et al., 2017), stochastic weather generation (e.g., Oriani et al., 2017;
44 Wojcik et al., 2009), geomorphological classification (e.g., Vannamettee et al., 2014) and
45 climate model downscaling (a domain that has typically been the realm of kriging-based
46 methods (e.g., Bancheri et al., 2018; Jha et al., 2015; Latombe et al., 2018)).

47 In the world of MPS simulations, one can distinguish two types of approaches. The first
48 category is the patch-based methods, where complete patches of the training image are imported
49 into the simulation. This category includes methods such as SIMPAT (Arpat and Caers, 2007)
50 and DISPAT (Honarkhah and Caers, 2010), which are based on building databases of patterns,
51 and image quilting (Mahmud et al., 2014), which uses an overlap area to identify patch
52 candidates, which are subsequently assembled using an optimal cut. CCSIM (Tahmasebi et al.,
53 2012) uses cross-correlation to rapidly identify optimal candidates. More recently, Li (2016)
54 proposed a solution that uses graph-cuts to find an optimal cut between patches, which has the
55 advantage of operating easily and efficiently independently of the dimensionality of the
56 problem. Tahmasebi (2017) propose as a solution that is based on “warping” in which the new
57 patch is distorted to match the previously simulated areas. For a multivariate simulation with
58 an informed variable, Hoffmann (2017) presented an approach for selecting a good candidate
59 based on the mismatch of the primary variable, and on the mismatch rank of the candidate
60 patches for auxiliary variables. Although patch-based approaches are recognized to be fast, they
61 typically suffer from a lack of variability due to the pasting of large areas of the training image,
62 which is a phenomenon that is called verbatim copy. Furthermore, patch-based approaches are
63 typically difficult to use in the presence of dense conditioning data.

64 The second category of MPS simulation algorithms consists of pixel-based algorithms, which
65 import a single pixel at the time instead of full patches. These methods are typically slower than
66 patch-based methods. However, they do not require a procedure for the fusion of patches, such
67 as an optimal cut, and they allow more flexibility in handling conditioning data. Furthermore,
68 in contrast to patch-based methods, pixel-based approaches rarely produce artifacts when
69 dealing with complex structures. The first pixel-based MPS simulation algorithm was
70 ENESIM, which was proposed by Guardiano and Srivastava, 1993, where for a given
71 categorical neighborhood – usually small – all possible matches in the training image are
72 searched. The conditional distribution of the pixel to be simulated is estimated based on all
73 matches, from which a value is sampled. This approach could originally handle only a few
74 neighbors and a relatively small training image; otherwise, the computational cost would
75 become prohibitive and the number of samples insufficient for estimating the conditional
76 distribution. Inspired by research in computer graphics, where similar techniques are developed
77 for texture synthesis (Mariethoz and Lefebvre, 2014), an important advance was the
78 development of SNESIM (Strebelle, 2002), which proposes storing in advance all possible
79 conditional distributions in a tree structure and using a multigrid simulation path to handle large



80 structures. With IMPALA, Straubhaar (2011) proposed reducing the memory cost by storing
81 information in lists rather than in trees. Another approach is direct sampling (DS) (Mariethoz
82 et al., 2010), where the estimation and the sampling of the conditional probability distribution
83 are bypassed by sampling directly in the training image, which incurs a very low memory cost.
84 DS enabled the first use of pixel-based simulations with continuous variables. DS can use any
85 distance formulation between two patterns; hence, it is well suited for handling various types
86 of variables and multivariate simulations.

87 In addition to its advantages, DS has several shortcomings: DS requires a threshold – which is
88 specified by the user – that enables the algorithm to differentiate good candidate pixels in the
89 training image from bad ones based on a predefined distance function. This threshold can be
90 highly sensitive and difficult to determine and often dramatically affects the computation time.
91 This results in unpredictable computation times, as demonstrated by Meerschman (2013). DS
92 is based on the strategy of randomly searching the training image until a good candidate is
93 identified (Shannon, 1948). This strategy is an advantage of DS; however, it can also be seen
94 as a weakness in the context of modern computer architectures. Indeed, random memory access
95 and high conditionality can cause 1) suboptimal use of the instruction pipeline, 2) poor memory
96 prefetch, 3) substantial reduction of the useful memory bandwidth and 4) impossibility of using
97 vectorization (John Paul Shen, 2018). While the first two problems can be addressed with
98 modern compilers and pseudorandom sequences, the last two are inherent to the current
99 memory and CPU construction.

100 This paper presents a new and flexible pixel-based simulation approach, namely, Quantile
101 Sampling (QS), which makes efficient use of modern hardware. Our method takes advantage
102 of the possibility of decomposing the standard distance metrics that are used in MPS (L^0 , L^2) as
103 sums of cross-correlations. As a result, we can use fast Fourier transforms (FFTs) to quickly
104 compute mismatch maps. To rapidly select candidate patterns in the mismatch maps, we use an
105 optimized partial sorting algorithm. A free, open-source and flexible implementation of QS is
106 available, which is interfaced with most common programming languages (C/C++, MATLAB,
107 R, and Python 3).

108 The remainder of this paper is structured as follows: Section 2 presents the proposed algorithm
109 with an introduction to the general method of sequential simulation, the mismatch measurement
110 using FFTs and the sampling approach of using partial sorting followed by methodological and
111 implementation optimizations. Section 3 evaluates the approach in terms of quantitative and
112 qualitative metrics via simulations and conducts benchmark tests against DS, which is the only
113 other available approach that can handle continuous pixel-based simulations. Section 4
114 discusses the strengths and weaknesses of QS and provides guidelines. Finally, guidelines and
115 the conclusions of this work are presented in Section 5.



116 2. Methodology and Implementation

117 2.1. Pixel-based sequential simulation

118 We recall the main structure of pixel-based MPS simulation algorithms (Mariethoz and Caers,
119 2014, p.156), which is summarized and adapted for QS in Pseudocode 1. The key difference
120 between existing approaches is in lines 3 and 4 of Pseudocode 1, when candidate patterns are
121 selected. This task is the most time-consuming in many MPS algorithms and we focus only on
122 computing it in a way that reduces its cost and minimizes the parameterization.

123

124 Pseudocode 1: QS Algorithm

125

126 Inputs:

127 T the training images

128 S the simulation grid, including the conditioning data

129 P the simulation path

130 The choice of pattern metric

131

- 132 1. **For** each unsimulated pixel x following the path P :
- 133 2. Find the neighborhood $N(x)$ in S that contains all previously simulated or conditioning
134 nodes in a specified radius
- 135 3. Compute the mismatch map between T and $N(x)$: [Section 2.3](#)
- 136 4. Select a good candidate using quantile sorting over the mismatch map: [Section 2.4](#)
- 137 5. Assign the value of the selected candidate to x in S
- 138 6. **End**

139

140 2.2. Decomposition of common mismatch metrics as sums of products

141 Distance-based MPS approaches are based on pattern matching (Mariethoz and Lefebvre,
142 2014). Here, we rely on the observation that many common matching metrics can be expressed
143 as weighted sums of the pixelwise mismatch ε . This section explores the pixelwise errors for a
144 single variable and for multiple variables. For a single variable, the mismatch metric ε between
145 two pixels is the distance between two scalars or two classes. In the case of many variables, it
146 is a distance between two vectors that are composed by scalars, by classes, or by a combination
147 of the two. Here, we focus on distance metrics that can be expressed in the following form:

148

Equation 1



149
$$\varepsilon(a, b) \propto \sum_j f_j(a) \cdot g_j(b)$$

150 where a and b represent the values of two univariate pixels and f_j and g_j are functions that
151 depend on the chosen metric. Here, we use the proportion symbol because we are interested in
152 relative metrics rather than absolute metrics, namely, the objective is to rank the candidate
153 patterns. We show below that many of the common metrics or distances that are used in MPS
154 can be expressed as Equation 1.

155 For the simulation of continuous variables, the most commonly used mismatch metric is the L^2 -
156 norm, which can be expressed as follows:

157 *Equation 2*

158
$$\varepsilon_{L^2}(a, b) = (a - b)^2 = a^2 - 2ab + b^2$$

159 Using Equation 1, this L^2 -norm can be decomposed into the following series of functions f_j and
160 g_j :

161	$f_0: x \rightarrow x^2$	164	$g_0: x \rightarrow 1$
162	$f_1: x \rightarrow -2x$	165	$g_1: x \rightarrow x$
163	$f_2: x \rightarrow 1$	166	$g_2: x \rightarrow x^2$

167

168



169

170 A similar decomposition is possible for the L^0 -norm (also called Hamming distance), which is
171 commonly used for the simulation of categorical variables. This measure of dissimilarity counts
172 the number of nonzero values in a vector (Hamming, 1950)

173

Equation 3

$$174 \quad \varepsilon_{L^0}(a, b) = (a - b)^0 = \sum_{j \in \mathcal{C}} 1 - (\delta_{a,j} \cdot \delta_{b,j}) \propto \sum_{j \in \mathcal{C}} \delta_{a,j} \cdot \delta_{b,j}$$

175 where $\delta_{x,y}$ is the Kronecker delta between x and y , which is equal to 1 if x equals y and 0
176 otherwise, and \mathcal{C} is the set of all possible categories of a specified variable.

177 Using Equation 1, this L^0 distance can be decomposed (Arpat and Caers, 2007) into the
178 following series of functions f_j and g_j :

$$179 \quad f_j: x \rightarrow -\delta_{xj}$$

$$180 \quad g_j: x \rightarrow \delta_{xj}$$

181 with a new pair of f_j and g_j for each class j of \mathcal{C} .

182 For multivariate pixels, such as a combination of categorical and continuous values, the
183 mismatch ε can be expressed as a sum of univariate pixelwise mismatches.

184

Equation 4

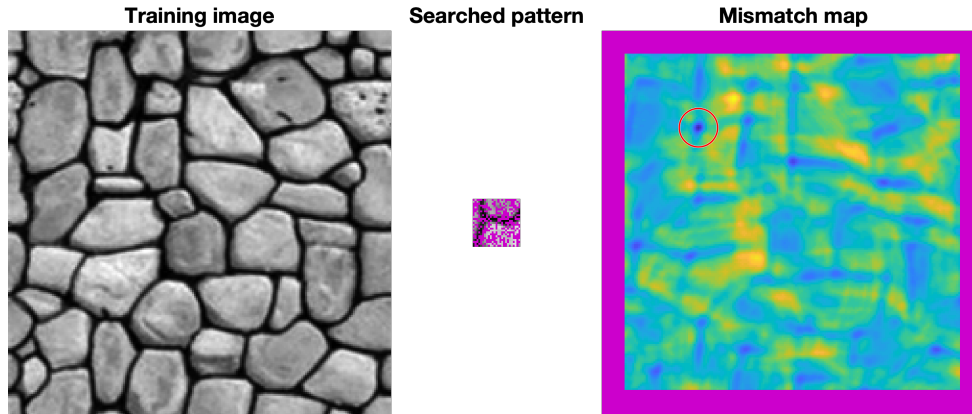
$$185 \quad \varepsilon(\mathbf{a}, \mathbf{b}) \propto \sum_i \sum_j f_j(a_i) \cdot g_j(b_i)$$

186 where \mathbf{a} and \mathbf{b} are the compared vectors and a_i and b_i are the individual components of \mathbf{a} and
187 \mathbf{b} .

188

189 **2.3. Computation of a mismatch map for an entire pattern**

190 The approach that is proposed in this work is based on computing a mismatch map in the TI for
191 each simulated pixel. The mismatch map is a grid that represents the pattern-wise mismatch for
192 each location of the training image and enables the fast identification of a good candidate, as
193 shown by the red circle in Figure 1.



194

195

196

197

Figure 1 Example of a mismatch map for an incomplete pattern. Blue represents good matches and yellow bad matches. The red circle highlights the minimum of the mismatch map, which corresponds to the location of the best candidate.

198

199 If we consider the neighborhood $N(s)$ around the simulated position s , then we can express a
 200 weighted dissimilarity between $N(s)$ and a location in the TI $N(t)$:

201

Equation 5

202

$$E(N(t), N(s)) = \sum_{\mathbf{l} | N_{\mathbf{l}}(t) \text{ and } N_{\mathbf{l}}(s) \text{ exist}} \omega_{\mathbf{l}} \varepsilon(N_{\mathbf{l}}(t), N_{\mathbf{l}}(s))$$

203

where $N_{\mathbf{l}}(p)$ is the ensemble of neighbors of p (p can represent either s or t), \mathbf{l} is the lag vector
 204 that defines the relative position of each value within N , and $\omega_{\mathbf{l}}$ is a weight for each pixelwise
 205 error according to the lag vector \mathbf{l} . By extension, ω is the matrix of all weights, which we call
 206 the weighting kernel or, simply, the kernel. E represents the mismatch between patterns that are
 207 centered on s and $t \in T$, where T is the training image.

208

Some lags may not correspond to a value, for example, due to edge effects in the considered
 209 images or because the patterns are incomplete. Missing patterns are inevitable during the course
 210 of a simulation using a sequential path. Furthermore, in many instances, there can be missing
 211 areas in the training image. This is addressed by creating an indicator variable to be used as a
 212 mask, which equals 1 at informed pixels and 0 everywhere else:

213

Equation 6

214

$$\mathbb{1}_{\mathbf{l}}(p) = \begin{cases} 1 & \text{if } N_{\mathbf{l}}(p) \text{ is informed} \\ 0 & \text{otherwise} \end{cases}$$

215

Let us first consider the case in which for a specified position, either all or no variables are
 216 informed. Expressing the presence of data as a mask enables the gaps to be ignored because the
 217 corresponding errors are multiplied by zero.

218

Then, Equation 5 can be expressed as follows:

219

Equation 7



$$220 \quad E(N(t), N(s)) = \sum_l \omega_l \cdot \mathbb{1}_l(t) \cdot \mathbb{1}_l(s) \cdot \varepsilon(N_l(t), N_l(s))$$

221 . Combining Equation 4 and Equation 7, we get:

222 *Equation 8*

$$224 \quad E(N(t), N(s)) \propto \sum_l \omega_l \cdot \mathbb{1}_l(t) \cdot \mathbb{1}_l(s) \sum_j \sum_i f_j(N_l(t)_i) \cdot g_j(N_l(s)_i)$$

$$225 \quad = \sum_l \sum_j \sum_i \omega_l \cdot \mathbb{1}_l(t) \cdot \mathbb{1}_l(s) \cdot f_j(N_l(t)_i) \cdot g_j(N_l(s)_i)$$

$$226 \quad = \sum_i \sum_j \sum_l \omega_l \cdot (\mathbb{1}_l(t) \cdot f_j(N_l(t)_i)) \cdot (\mathbb{1}_l(s) \cdot g_j(N_l(s)_i))$$

223 .

227 After rewriting and reordering, Equation 8 can be expressed as a sum of cross-correlations that
 228 encapsulate spatial dependencies:

229 *Equation 9*

$$230 \quad E(N(t), N(s)) \propto \sum_i \sum_j (\mathbb{1}(t) \circ f_j(N(t)_i)) \star (\omega \circ \mathbb{1}(s) \circ g_j(N(s)_i))$$

231 , where ω and $\mathbb{1}(\cdot)$ represent the matrices that are formed by ω_l and $\mathbb{1}_l(\cdot)$ for all possible vectors
 232 l , \star denotes the cross-correlation operator, and \circ is the element-wise product (or Hadamard-
 233 product).

234 Finally, by applying cross-correlations for all positions $t \in T$, we obtain a mismatch map,
 235 which is expressed as:

236 *Equation 10*

$$237 \quad E(T, N(s)) \propto \sum_i \sum_j (\mathbb{1}(T) \circ f_j(T_i)) \star (\omega \circ \mathbb{1}(s) \circ g_j(N(s)_i))$$

238 . The term $\mathbb{1}(T)$ allows the consideration of the possibility of missing data in the training image
 239 T .

240 Let us consider the general case in which only some variables are informed and the weighting
 241 can vary for each variable. Equation 10 can be extended for this case by defining separate masks
 242 and weights ω_i for each variable:

243 *Equation 11*

$$244 \quad E(T, N(s)) \propto \sum_i \sum_j (\mathbb{1}(T_i) \circ f_j(T_i)) \star (\omega_i \circ \mathbb{1}(s_i) \circ g_j(N(s)_i))$$

245 . Equation 11 can be expressed using the convolution theorem:

246 *Equation 12*



$$247 \quad E(T, N(s)) \propto \sum_i \sum_j \mathcal{F}^{-1} \left\{ \overline{\mathcal{F}\{\mathbb{1}(T_i) \circ f_j(T_i)\}} \circ \mathcal{F}\{\omega_i \circ \mathbb{1}(s_i) \circ g_j(N(s)_i)\} \right\}$$

248 , where \mathcal{F} represents the Fourier transform, \mathcal{F}^{-1} the inverse transform, and \bar{x} the conjugate of
249 x .

250 By linearity of the Fourier transform, the summation can be performed in Fourier space, thereby
251 reducing the number of transformations:

252 *Equation 13*

$$253 \quad E(T, N(s)) \propto \mathcal{F}^{-1} \left\{ \sum_i \sum_j \overline{\mathcal{F}\{\mathbb{1}(T_i) \circ f_j(T_i)\}} \circ \mathcal{F}\{\omega_i \circ \mathbb{1}(s_i) \circ g_j(N(s)_i)\} \right\}$$

254 . Equation 13 is appropriate for modern computers, which are well-suited for computing FFTs
255 (Cooley et al., 1965; Gauss, 1799). Currently, FFTs are well implemented in highly optimized
256 libraries (Rodríguez, 2002). Equation 13 is the expression that is used in our QS implementation
257 because it reduces the number of Fourier transforms, which are the most computationally
258 expensive operations of the algorithm. One issue with the use of FFTs is that the image T is
259 typically assumed to be periodic. However, in most practical applications, it is not periodic.
260 This can be simply addressed by cropping the edges of $E(T, N(s))$ or by adding a padding
261 around T .

262 The computation of the mismatch map (Equation 13) is deterministic; as a result, it incurs a
263 constant computational cost that is independent of the pixel values. Additionally, Equation 13
264 is expressed without any constraints on the dimensionality. Therefore, it is possible to use the
265 n -dimensional FFTs that are provided in the above libraries to perform n -dimensional
266 simulations without changing the implementation.

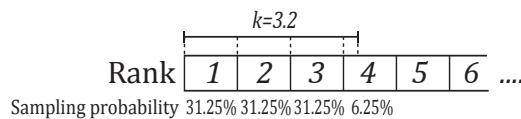
267 **2.4. Selection of candidates based on a quantile**

268 The second contribution of this work is the k -sampling strategy for selecting a simulated value
269 among candidates. The main idea is to use the previously calculated mismatch map to select a
270 set of potential candidates that are defined by the k smallest (i.e. a quantile) values of E . Once
271 this set has been selected, we randomly draw a sample from this pool of candidates. This differs
272 from strategies that rely on a fixed threshold, which can be cumbersome to determine. This
273 strategy is highly similar to the ε -replicate strategy that is used in image quilting (Mahmud et
274 al., 2014) in that we reuse and extend to satisfy the specific requirements of QS. It has the main
275 advantage of rescaling the acceptance criterion according to the difficulty; i.e. the algorithm is
276 more tolerant of rare patterns while requiring very close matches for common patterns.

277 In detail, the candidate selection procedure is as follows: All possible candidates are ranked
278 according to their mismatch and one candidate is randomly sampled among the k best. This
279 number k can be seen as a quantile over the training dataset. However, parameter k has the
280 advantage of being an easy representation for users, who can associate $k = 1$ with the best
281 candidate, $k = 2$ with the two best candidates, etc. For fine-tuning parameter k , the sampling



282 strategy can be extended to noninteger values of k by sampling the candidates with probabilities
 283 that are not uniform. For example, if the user sets $k = 1.5$, the best candidate has a probability
 284 of $2/3$ of being sampled and the second best a probability of $1/3$. For $k = 3.2$, (Figure 2) each
 285 of the 3 best candidates are sampled with an equal probability of 0.3125 and the 4th best with a
 286 probability of 0.0625. This feature is especially useful for tuning k between 1 and 2 and for
 287 avoiding a value of $k = 1$, which can result in the phenomenon of verbatim copy.



288

289 *Figure 2 Illustration of the k -sampling strategy*

290 An alternative sampling strategy for reducing the simulation time is presented in Appendix A.3.
 291 However, this strategy can result in a reduction in the simulation quality.

292

293 **2.5. Simplifications in the case of a fully informed training image**

294 In many applications, spatially exhaustive TIs are available. In such cases, the equations above
 295 can be simplified by dropping constant terms from Equation 1, thereby resulting in a simplified
 296 form for Equation 13. Here, we take advantage of the ranking to know that a constant term will
 297 not affect the result.

298 As in Tahmasebi (2012), in the L^2 -norm, we drop the squared value of the searched pattern,
 299 namely, b^2 , from Equation 2. Hence, we can express Equation 4 as follows:

300

Equation 14

301

$$\varepsilon(\mathbf{a}, \mathbf{b}) = \sum_i a_i^2 - 2 \sum_i a_i \cdot b_i$$

302 The term a^2 , which represents the squared value of the candidate pattern in the TI, differs
 303 among training image locations and, therefore, cannot be removed. Indeed, the assumption that
 304 $\sum a^2$ is constant is only valid under a strict stationarity hypothesis on the scale of the search
 305 pattern. While this hypothesis might be satisfied in some cases (as in Tahmasebi et al., 2012),
 306 we do not believe it is generally valid. Via the same approach, Equation 3 can be simplified by
 307 removing the constant terms; then, we obtain the following for the L^0 -norm:

308

Equation 15

309

$$\varepsilon(\mathbf{a}, \mathbf{b}) = - \sum_{j \in \mathcal{C}} \sum_i \delta_{a_i, j} \cdot \delta_{b_i, j}$$

310



311 2.6. Efficient Implementation

312 An efficient implementation of QS was achieved by 1) performing precomputations, 2)
313 implementing an optimal partial sorting algorithm for selecting candidates and 3) optimal
314 coding and compilation. These are described below.

315 According to Equation 13, $\overline{\mathcal{F}\{\mathbb{1}(T_i) \circ f_j(T_i)\}}$ is independent of the searched pattern $N(s)$.
316 Therefore, it is possible to precompute it at the initialization stage for all i and j . This
317 improvement typically reduces the computation time for an MPS simulation by a factor of at
318 least 2.

319 In the QS algorithm, a substantial part of the computation cost is incurred in identifying the k
320 best candidates in the mismatch map. In the case of noninteger k , the upper limit $\lceil k \rceil$ is used.
321 Identifying the best candidates requires sorting the values of the mismatch map and retaining
322 the candidates in the top k ranks. For this, an efficient sorting algorithm is needed. The
323 operation of finding the k best candidates can be implemented with a partial sort, in which only
324 the elements of interest are sorted, while the other elements remain unordered. This results in
325 two sets: \mathfrak{S}_s with the k smallest elements and \mathfrak{S}_l with the largest elements. The partial sort
326 guarantees that $x \leq y \mid (x, y) \in \mathfrak{S}_s \times \mathfrak{S}_l$. More information about our implementation of this
327 algorithm is available in Appendix A.1. Here, we use a modified vectorized online heap-based
328 partial sort (Appendix A.1). With a complexity of $O(n \cdot \ln(k))$, it is especially suitable for small
329 values of k . Using the cache effect, the current implementation yields results that are close to
330 the search of the best value (the smallest value of the array). The main limitation of standard
331 partial sort implementations is that in the case of equal values, either the first or the last element
332 is sampled. Here, we develop an implementation that can uniformly sample a position among
333 similar values with a single scan of the array. This is important because systematically selecting
334 the same position for the same pattern will reduce the conditional probability density function
335 to a unique sample, thereby biasing the simulation.

336 Due to the intensive memory access by repeatedly scanning large training images, interpreted
337 programming languages, such as MATLAB and Python, are inefficient for a QS
338 implementation and, in particular, for a parallelized implementation. We provide a NUMA-
339 aware and flexible C/C++/OpenMP implementation of QS that is highly optimized. Following
340 the denomination of Mariethoz (2010), we use a path-level parallelization with a waiting
341 strategy, which offers a good trade-off between performance and memory requirements. In
342 addition, two node-level parallelization strategies are available: if many training images are
343 used, a first parallelization is performed over the exploration of the training images; then, each
344 FFT of the algorithm is parallelized using natively parallel FFT libraries.

345 The FFTw library (Frigo and Johnson, 2018) provides a flexible and performant architecture-
346 independent framework for computing n -dimensional Fourier transformations. However, an
347 additional speed gain of approximately 20% was measured by using the Intel MKL library (Intel
348 Corporation, 2019) on compatible architectures. We also have a GPU implementation that uses
349 clFFT for compatibility. Many Fourier transforms are sparse and, therefore, can easily be



350 accelerated in n -dimensional cases with “partial FFT” since Fourier transforms of only zeros
351 result in zeros.

352 **3. Results**

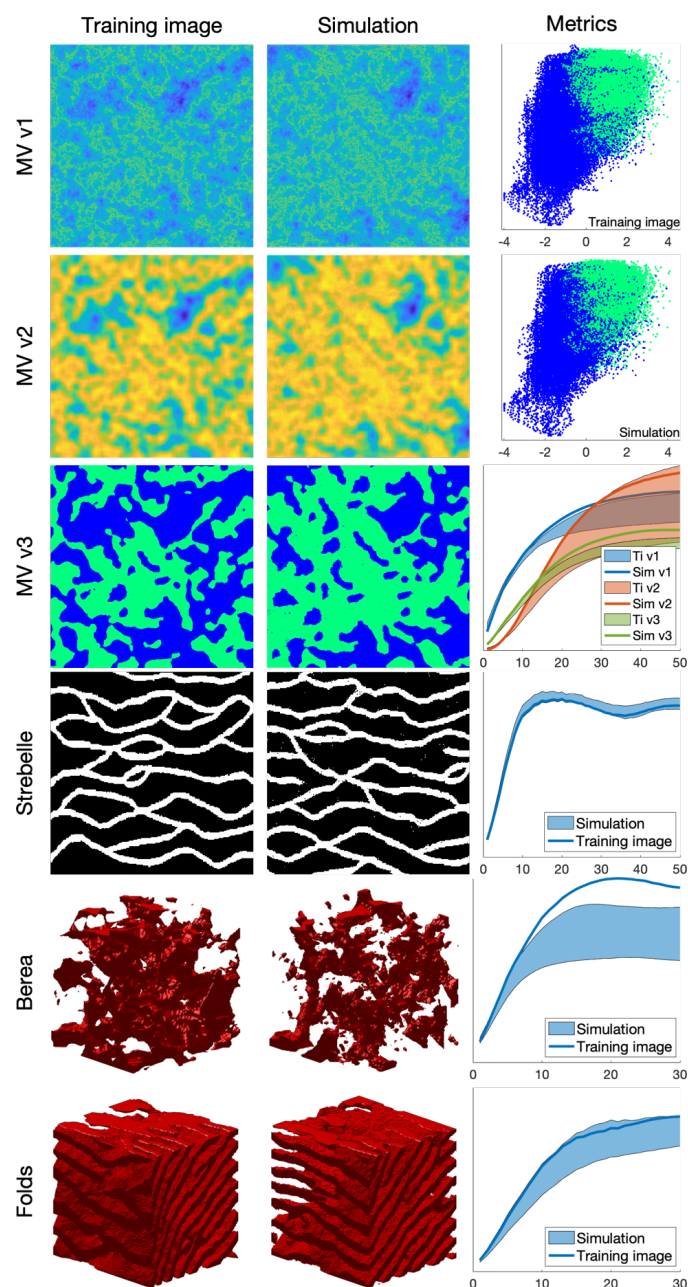
353 **3.1. Simulation examples**

354 This section presents illustrative examples for continuous and categorical case studies in 2D
355 and in 3D. Additional tests are reported in Appendix 0. The parameters that are used for the
356 simulations of Figure 3 are reported in Table 1.

357 The results show that simulations results are consistent with what is typically observed with
358 state-of-the-art MPS algorithms. While simulations can accurately reproduce TI properties for
359 relatively standard examples with repetitive structures (e.g., MV, Strebelle, and Folds), training
360 images with long-range features (typically larger than the size of the TI) are more difficult to
361 reproduce, such as in the Berea example. For multivariate simulations, the reproduction of the
362 joint distribution is satisfactory, as observed in the scatter plots (Figure 3).

363

364



365
 366
 367
 368
 369
 370
 371
 372

Figure 3 Examples of unconditional continuous and categorical simulations in 2D and 3D and their variograms. The first column shows the training images that were used, the second column one realization, and the third column quantitative quality metrics. MVs v1, v2 and v3 represent a multivariate training image (and the corresponding simulation) using 3 variables. The first two metrics are scatter plots of MV v1 vs. MV v2 of the training image and the simulation, respectively. The third metric represents the reproduction of the variogram for each of MVs v1, v2 and v3.



373

	MVs v1, v2, v3	Strebelle	Berea	Folds
Source	(Mariethoz and Caers, 2014)	(Strebelle, 2002)	Doi:10.6084/m9.figshare.1153794	(Mariethoz and Caers, 2014)
Size of the training image (px)	490 × 490	250 × 250	100 × 100 × 100	180 × 150 × 120
Size of the simulation (px)	490 × 490	250 × 250	100 × 100 × 100	180 × 150 × 120
Computation time (s)	1456	54	1665	76270
k	1.2			
N	80		125	

374 *Table 1 Parameters that were used for the simulations in Figure 3. Times are specified for*
 375 *simulations without parallelization.*

376 3.2. Comparison with direct sampling simulations

377 QS simulations are benchmarked against DS using the “Stone” training image (Figure 4). The
 378 settings that are used for DS are based on optimal parameters that were obtained via the
 379 approach of Baninajar et al. (2019), which uses stochastic optimization to find optimal
 380 parameters. In DS, we use a fraction of scanned TI of $f = 1$ to explore the entire training image
 381 via the same approach as in QS and we use the L^2 -norm as in QS. To avoid the occurrence of
 382 verbatim copy, we include 0.1% conditioning data, which are randomly sampled from a rotated
 383 version of the training image. The number of neighbors N is set to 20 for both DS and QS and
 384 the acceptance threshold of DS is set to 0.001.

385 The comparison is based on qualitative (Figure 5) and quantitative (Figure 6) metrics, which
 386 include directional and omnidirectional variograms, along with the connectivity function and
 387 the Euler characteristic (Renard and Allard, 2013). The results demonstrate that the simulations
 388 are of a quality that is comparable to DS. With extreme settings (highest pattern reproduction
 389 regardless of the computation time), both algorithms perform similarly, which is reasonable
 390 since both are based on sequential simulation and both directly import data from the training
 391 image.

392 With QS, kernel weighting enables the adaption of the parametrization to improve the results,
 393 as shown in Figure 5. In this paper, we use an exponential kernel:

394

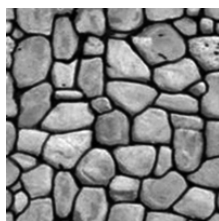
Equation 16

395

$$\omega_l = e^{-\alpha \|l\|_2}$$



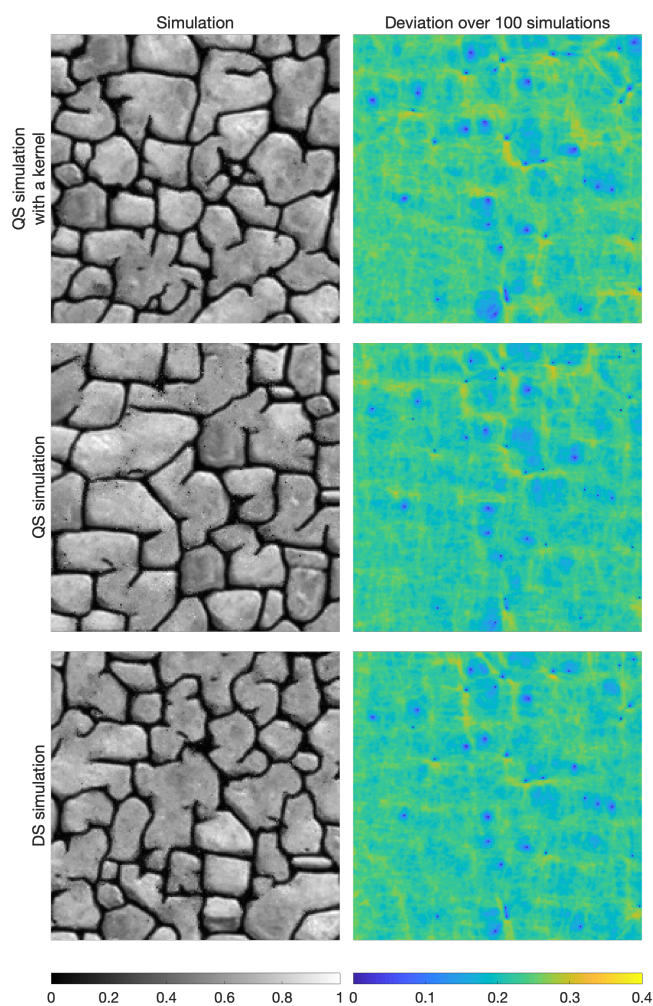
396 where α is a kernel parameter. The validation metrics of Figure 6 show that both QS and DS
397 tend to slightly underestimate the variance and the connectivity. Figure 6 shows that an optimal
398 kernel improves the results for all metrics, with all training image metrics in the 5-95%
399 realization interval, except for the Euler characteristic.



400

401

Figure 4 Training image that was used for benchmarking and sensitivity analysis.

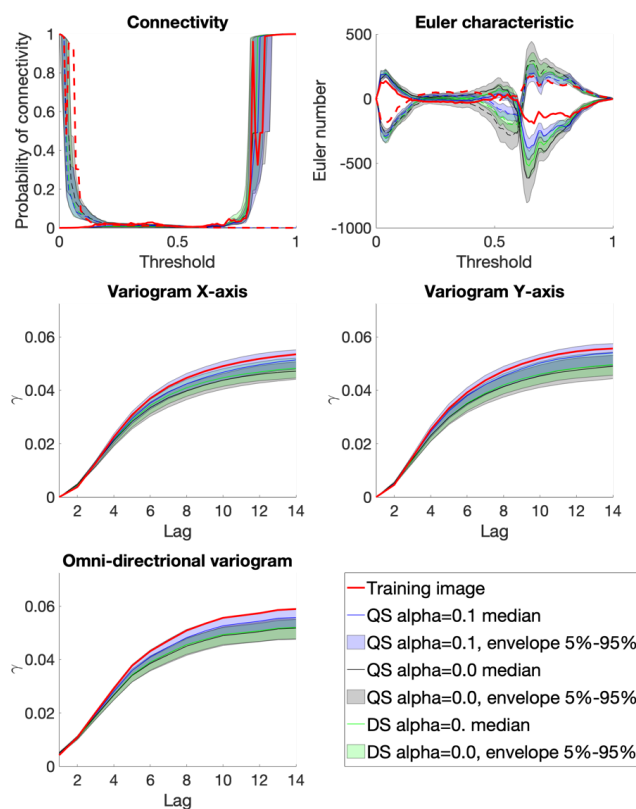


402

403

404

Figure 5 Examples of conditional simulations and their standard deviation over 100 realizations that are used in the benchmark between QS and DS.



405

406

Figure 6 Benchmark between QS and DS over 5 metrics.

407

3.3. Parameter sensitivity analysis

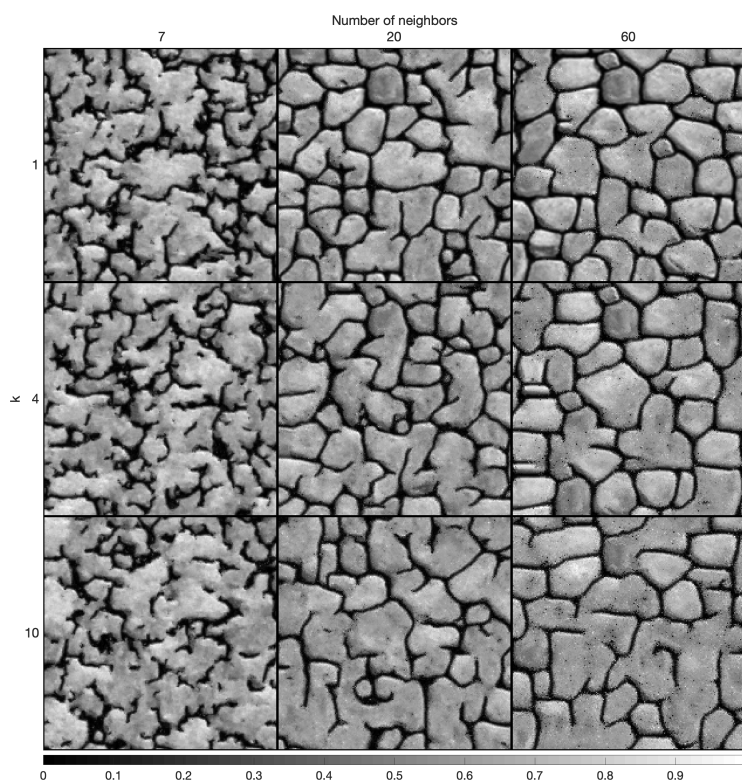
408

In this section, we perform a sensitivity analysis on the parameters of QS using the training image in Figure 4. Only essential results are reported in this section (Figure 7 and Figure 8); more exhaustive test results are available in Appendix 0 (Figure A 4 and Figure A 5). The two main parameters of QS are the number of neighbors N and the number of used candidates k .

412

Figure 7 (and Appendix 0 Figure A 4) shows that large N values and small k values improve the simulation performance; however, tend to induce verbatim copy in the simulation. Small values of N result in noise with good reproduction of the histogram.

414



415

416

417

Figure 7 Sensitivity analysis on one simulation for the two main parameters of QS using a uniform kernel.

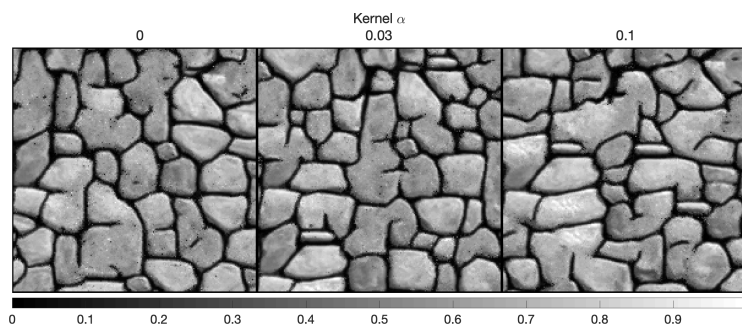
418

ω can be a very powerful tool, typically using the assumption that the closest pixels are more informative than remote pixels. The results of study of the effect of the kernel value α are explored in Figure 8 and Figure A 5, which shows that α provides a unique tool for improving the quality of the simulation.

419

420

421



422

423

Figure 8 Sensitivity analysis on the kernel parameter α , with fixed parameters $k=1.5$ and $N=40$.

424



425 3.4. Computational efficiency and scalability

426 In this section, we investigate the scalability of QS with respect to the size of the simulation
427 grid, the size of the training image grid, the number of variables, incomplete training images,
428 and hardware. According to the test results, the code will continue to scale with new-generation
429 hardware.

430 As explained in Section 2.3 and 2.4, the amounts of time that are consumed by the two main
431 operations of QS (finding candidates and sorting them) are independent of the pixel values.
432 Therefore, the training image that is used is not relevant (here, we use simulations that were
433 performed with the TI of Figure 4 and its classified version for categorical cases). Furthermore,
434 the computation time is independent of the parametrization (k and N). However, the
435 performance is affected by the type of mismatch function that is used; here, we consider both
436 continuous (Equation 2 and Equation 14) and categorical cases (Equation 3 and Equation 15).

437 We also test our implementation on different types of hardware, as summarized in Table 2. We
438 expect Machine (2) to be faster than Machine (1) for medium-sized problems due to the high
439 memory bandwidth requirement of QS. Machine (3) should also be faster than Machine (1)
440 because it takes advantage of a longer vector computation (512-bit VS. 256-bit instruction set).

Name of the machine	Machine (1)	Machine (2)	Machine (3)
CPU	-2x Intel(R) Xeon(R) CPU E5-2680 v2 @ 2.80 GHz	-Xeon Phi, Intel(R) Xeon Phi (TM) CPU 7210 @ 1.30 GHz	-2x Intel(R) Xeon(R) Gold 6128 Processor @ 3.40 GHz
Memory type	- DDR3	- MCDRAM / DDR4	- DDR4
OS, compiler and compilation flags	Linux, Intel C/C++ compiler 2018 with -xhost		

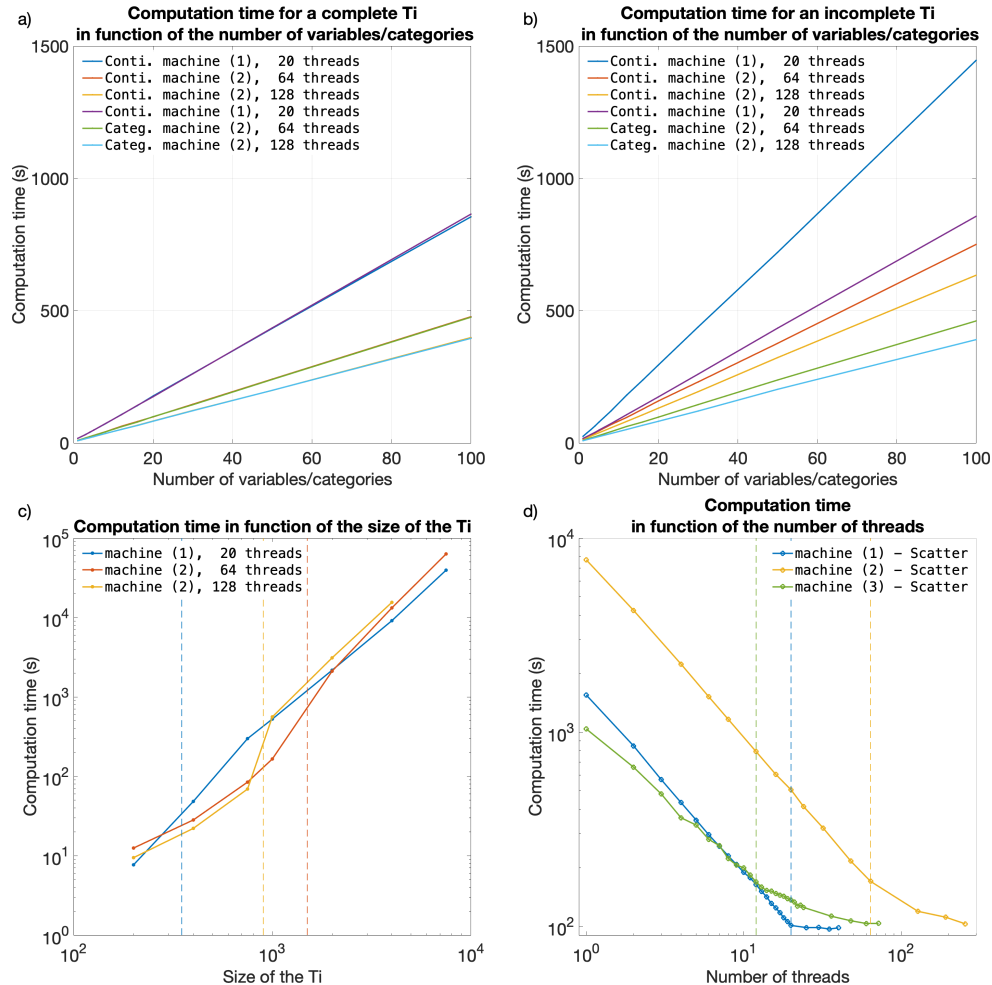
441 *Table 2 Hardware that was used in the experiments*

442 Figure 9 plots the execution times on the 3 tested machines for continuous and categorical cases
443 and with training images of various sizes. Since QS has a predictable execution time, the
444 influence of the parameters on the computation time is predictable: linear with respect to the
445 number of variables (Figure 9a, Figure 9b), linear with respect to the size of the simulation grid
446 and following a power function of the size of the training image (Figure 9c). Therefore, via a
447 few tests on a set of simulations, one can predict the computation time for any other setting.

448 Figure 9d shows the scalability of the algorithm when using the path-level parallelization. The
449 algorithm scales well until all physical cores are being used. Machine (3) has a different scaling
450 factor (slope). This suboptimal scaling is attributed to the limited memory bandwidth. Our
451 implementation of QS scales well with an increasing number of threads (Figure 9d), with an
452 efficiency above 80% using all possible threads. The path-level parallelization strategy that was
453 used involves a bottleneck for large number of threads due to the need to wait for neighborhood
454 conflicts to be resolved (Mariethoz 2010). This effect typically appears for large values of N or



455 intense parallelization (>50 threads) on small grids. It is assumed that small grids do not require
456 intense parallelization; hence, this problem is irrelevant in most applications.



457

458 *Figure 9 Efficiency of QS with respect to all key parameters. a) and b) are the evolutions of the*
459 *computation time for complete and incomplete training images, respectively, with continuous*
460 *and categorical variables. c) shows the evolution of the computation time as the size of the*
461 *training image is varied; the dashed lines indicate that the training image no longer fits in the*
462 *CPU cache. d) shows the evolution of the computation time as the number of threads is*
463 *increased. The dashed lines indicate that all physical cores are used.*

464

465 4. Discussion

466 The parameterization of the algorithm (and therefore simulation quality) has almost no impact
467 on the computational cost, which is an advantage. Indeed, many MPS algorithms impose trade-



468 offs between the computation time and the parameters that control the simulation quality,
469 thereby imposing difficult choices for the users. QS is comparatively simpler to set up in this
470 regard. In practice, a satisfactory parameterization strategy is often to start with a small k value
471 (say 1.2) and a large N value (> 50) and then gradually change these values to increase the
472 variability if necessary (Figure 6 and Figure A 4).

473 QS is adapted for simulating continuous variables using the L^2 -norm. However, a limitation is
474 that the L^1 -norm does not have a decomposition that satisfies Equation 1 and, therefore, cannot
475 be used with QS. Another limitation is that for categorical variables, each class requires a
476 separate FFT, which incurs an additional computational cost. This renders QS less
477 computationally efficient for categorical variables (if there are more than 2 categories) than for
478 continuous variables. For accelerated simulation of categorical variables, a possible alternative
479 to reduce the number of required operations is presented in Appendix A.2. The strategy is to
480 use encoded variables, which are decoded in the mismatch map. While this alternative yields
481 significant computational gains, it does not allow the use of a kernel weighting and is prone to
482 numerical precision issues.

483 The computational efficiency of QS is generally great compared to other pixel-based
484 algorithms: for example, in our tests it performed faster than DS. QS requires more memory
485 than DS, especially for applications with categorical variables with many classes and with a
486 path-level parallelization. However, the memory requirement is much lower compared to MPS
487 algorithms that are based on a pattern database, such as SNESIM.

488 There may be cases in which it is slower than DS, in particular when using a large training
489 image that is highly repetitive. In such cases, using DS can be advantageous as it must scan
490 only a very small part of the training image. For scenarios of this type, it is possible to adapt
491 QS such that only a small subset of the training image is used; this approach is described in
492 Appendix A3.

493 QS can be extended to handle the rotation and scaling of patterns by applying a constant rotation
494 or affinity transformation to the searched patterns (Strebelle, 2002). However, the use rotation-
495 invariant distances and affinity-invariant distances (as in Mariethoz and Kelly, 2011), while
496 possible in theory, would substantially increase the computation time. Mean-invariant distances
497 can be implemented by simply adapting the distance formulation in QS. All these advanced
498 features are outside the scope of this paper.

499 5. Conclusions

500 QS is an alternative approach for performing n -dimensional pixel-based simulations, which
501 uses an L^2 -distance for continuous cases and an L^0 -distance for categorical data. The framework
502 is highly flexible and allows other metrics to be used. The simple parameterization of QS
503 renders it easy to use for nonexpert users. Compared to other pixel-based approaches, QS has
504 the advantage of generating realizations in constant and predictable time for a specified training
505 image size. Using the quantile as a quality criterion naturally reduces the small-scale noise
506 compared to DS. In terms of parallelization, the QS code scales well and can adapt to new
507 architectures due to the use of external highly optimized libraries.



508 The QS framework provides a complete and explicit mismatch map, which can be used to
509 formulate problem-specific rules for sampling or even solutions that take the complete
510 conditional probability density function into account, for example, such as a narrowness
511 criterion for the conditional pdf of the simulated value (Gravey et al., 2019; Rasera et al., 2019),
512 or to use the mismatch map to infer the optimal parameters of the algorithm.

513 **6. Code availability**

514 The source code and documentation of the QS simulation algorithm are available as part of the
515 G2S package at: <https://github.com/GAIA-UNIL/G2S> under GPLv3 license. Or permanently
516 at <https://doi.org/10.5281/zenodo.3546338>

517 Platform: Linux / macOS / Windows 10 Language: C/C++

518 Interfacing functions in MATLAB, Python3, R

519 A package is available with our unbiased partial sort at:
520 <https://github.com/mgravey/randomKmin-max>

521 **7. Author contribution**

522 MG proposed the idea, implemented and optimized the QS approach and wrote the manuscript.
523 GM provided supervision, methodological insights and contributed to the writing of the
524 manuscript.

525 **8. Appendices**

526 **A.1. Partial sorting with random sampling**

527 Standard partial sorting algorithms resolve tie ranks deterministically, which does not accord
528 with the objective of stochastic simulation with QS, where variability is sought. Here, we
529 propose an online heap-based partial sort. It is realized with a single scan of the array of data
530 using a heap to store previously found values. This approach is especially suitable when we are
531 interested in a small fraction of the entire array.

532 Random positions of the k best values are ensured by swapping similar values. If $k = 1$, the
533 saved value is switched with a smaller value each time it is encountered. If an equal value is
534 scanned, a counter c is increased for this specific value and a probability of $1/c$ of switching to
535 the new position is applied. If $k > 1$, the same strategy is extended by carrying over the counter
536 c .

537 This partial sort outperforms random exploration of the mismatch map. However, it is difficult
538 to implement efficiently on GPUs. A solution is still possible for shared-memory GPUs by



539 performing the partial sort on the CPU. This is currently available in the proposed
540 implementation.

```
541 k: the number of values of interest
542 D: the input data array
543 S: the array with the k smallest values (sorted)
544 Sp: the array with the positions that are associated with the values of S
545
546 1. for each value v of D
547 2.   if v is smaller than the smallest value of S
548 3.     search in S for the position p at which to insert v and insert it
549 4.     if p = k // last position of the array
550 5.       reinitialize the counter c to 0
551 6.       insert v at the last position
552 7.     else
553 8.       increment c by one
554 9.       swap the last position with another of the same value
555 10.      insert the value at the expected position p
556 11.    end
557 12.  else if v is equal to the smallest value of S
558 13.    increment c by one
559 14.    change the position of v to one of the n positions of equal value with a probability of
560     $n/(n + c)$ 
561 15.  end
562 16. end
```

563 **A.2. Encoded categorical variables**

564 To handle categorical variables, a standard approach is to consider each category as an
565 independent variable. This requires as many FFTs as classes. This solution renders it expensive
566 to use QS in cases with multiple categories.

567 An alternative approach is to encode the categories and to decode the mismatch from the cross-
568 correlation. It has the advantage of only requiring only a single cross-correlation for each
569 simulated pattern.

570 Here, we propose encoding the categories as powers of the number of neighbors, such that their
571 product is equal to one if the class matches. In all other cases, the value is smaller than one or
572 larger than the number of neighbors.

$$573 \quad \varepsilon_{L^0}(a, b) = \psi((a - b)^0 \propto -(N + 1)^{-p(a)} \cdot (N + 1)^{-p(b)})$$

574 where N is the largest number of neighbors that can be considered and $p(c)$ is an arbitrary
575 function that maps index classes of \mathcal{C} , $c \in \mathcal{C}$.

576 In this scenario, in Equation 1 this encoded distance L_e^0 can be decomposed into the following
577 series of functions f_j and g_j :

$$578 \quad f_0: x \rightarrow -(N + 1)^{p(x)}$$



579 $g_0: x \rightarrow (N + 1)^{-p(x)}$

580 and the decoding function is

581
$$\psi(x) = [x] \bmod N$$

582 Table A 1 describes this process for 3 classes, namely, $a, b,$ and $c,$ and a maximum of 9
 583 neighbors. Then, the error can be easily decoded by removing decimals and dozens.

Products	$g_0(a) = 1$	$g_0(b) = 0.1$	$g_0(c) = 0.01$
$f_0(a) = 1$	1	0.1	0.01
$f_0(b) = 10$	10	1	0.1
$f_0(c) = 100$	100	10	1

584 *Table A 1 Example of encoding for 3 classes and 9 neighbors and their associated products*

585 Consider the following combination:

586 $f_0(a, \text{ } b, \text{ } a, \text{ } c, \text{ } c, \text{ } b, \text{ } a, \text{ } a, \text{ } b)$

587 $\times g_0(c, \text{ } b, \text{ } b, \text{ } a, \text{ } a, \text{ } b, \text{ } c, \text{ } a, \text{ } a)$

588
$$-(0.01, \text{ } 1, \text{ } 0.1, \text{ } 100, \text{ } 100, \text{ } 1, \text{ } 0.01, \text{ } 1, \text{ } 10) = -213.12$$

589 The decoding $[-213.12] \bmod 10 = -213 \bmod 10 = -3$ yields 3 matches (in green).

590 This encoding strategy provides the possibility of drastically reducing the number of FFT
 591 computations. However, the decoding phase is not always implementable if a nonuniform
 592 matrix ω is used. Finally, the test results show that the method suffers quickly from numerical
 593 precision issues, especially with many classes.

594 **A.3. Sampling strategy using training image splitting**

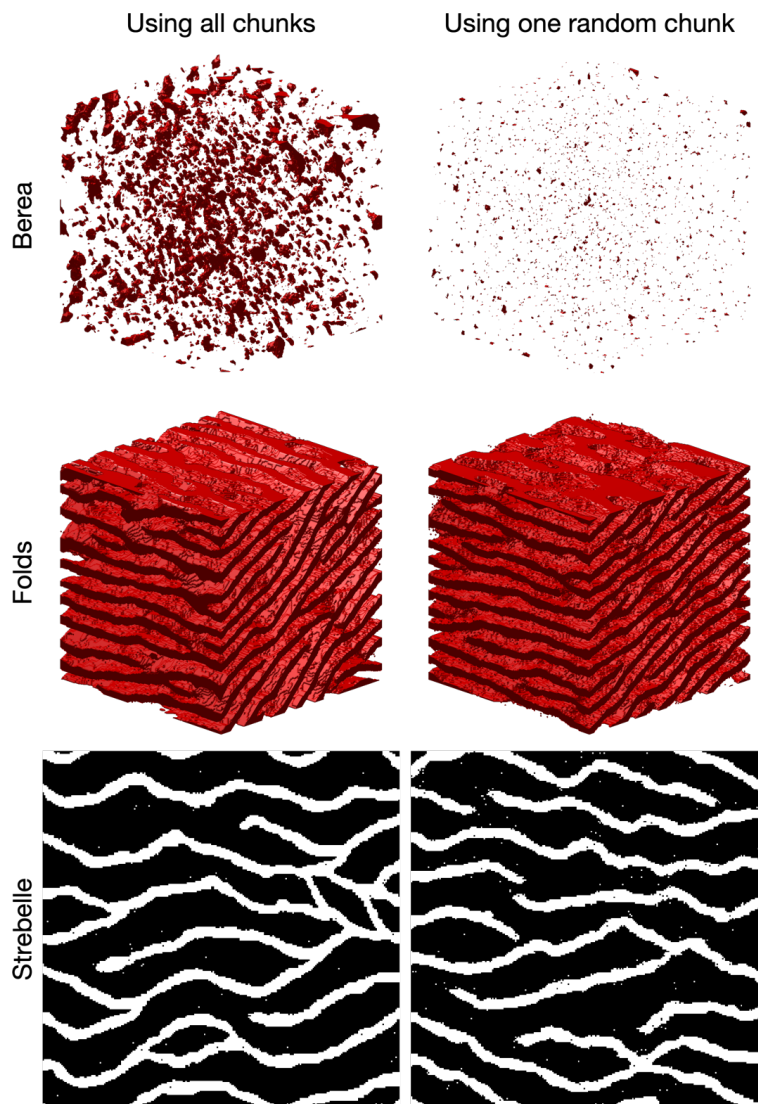
595 The principle of considering a fixed number of candidates can be extended by instead of taking
 596 the k^{th} best candidate, sampling the best candidate in only a portion $\frac{1}{k}$, of the TI. For instance,
 597 as an alternative to considering $k = 4,$ this strategy searches for the best candidate in one fourth
 598 of the image. This is more computationally efficient. However, if all the considered candidates
 599 are contiguous (by splitting the TI in k chunks), this approximation is only valid if the TI is
 600 completely stationary and all k equal subdivisions of the TI are statistically identical. In
 601 practice, real-world continuous variables are often nonstationary. However, in categorical
 602 cases, especially in binary ones, the number of pattern replicates is higher and this sampling
 603 strategy could be interesting.

604 The results of applying this strategy are presented in Table A 2 and Figure A 1. The
 605 experimental results demonstrate that the partial exploration approach that is provided by
 606 splitting substantially accelerates the processing time. However, Figure A 1 shows that the
 607 approach has clear limitations when dealing with training images with complex and



608 nonrepetitive patterns. The absence of local verbatim copy can explain the poor-quality
609 simulation results.

610



611

612 *Figure A 1 Comparison of QS using the entire training image and using training image*
613 *splitting. In these examples, the training image is split into two images over each dimension.*
614 *The original training images are presented in Figure 2.*

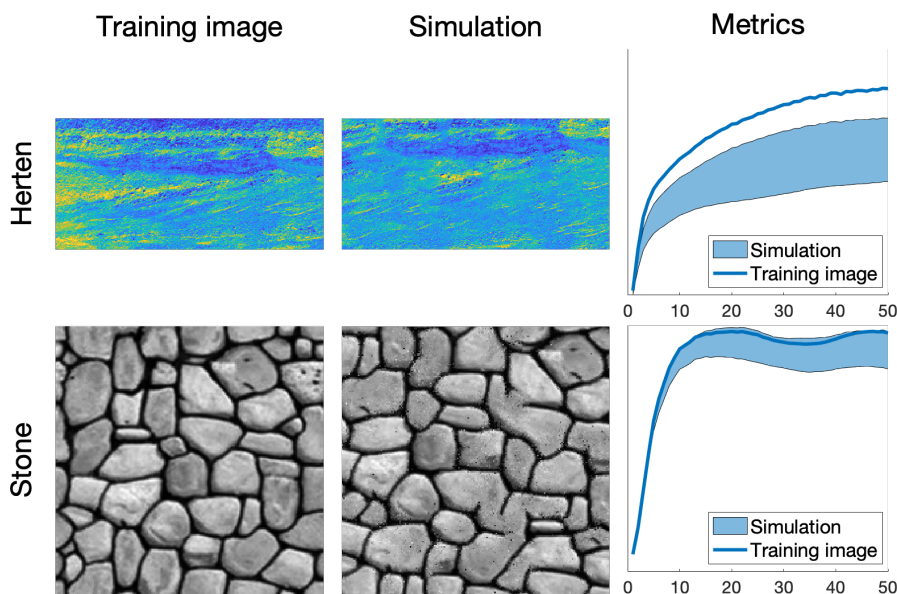
615



Training image	Using all chunks	Using one random chunk	Speedup
Berea	11 052 s	1 452 s	7.61x
Folds	35 211 s	4 063 s	8.66x
Strebelle	7.95 s	3.16 s	2.51x

616 *Table A 2 Computation times and speedups for the full and partial exploration approaches.*
 617 *Times are specified for simulations with path level parallelization.*

618 **A.4. Additional results**



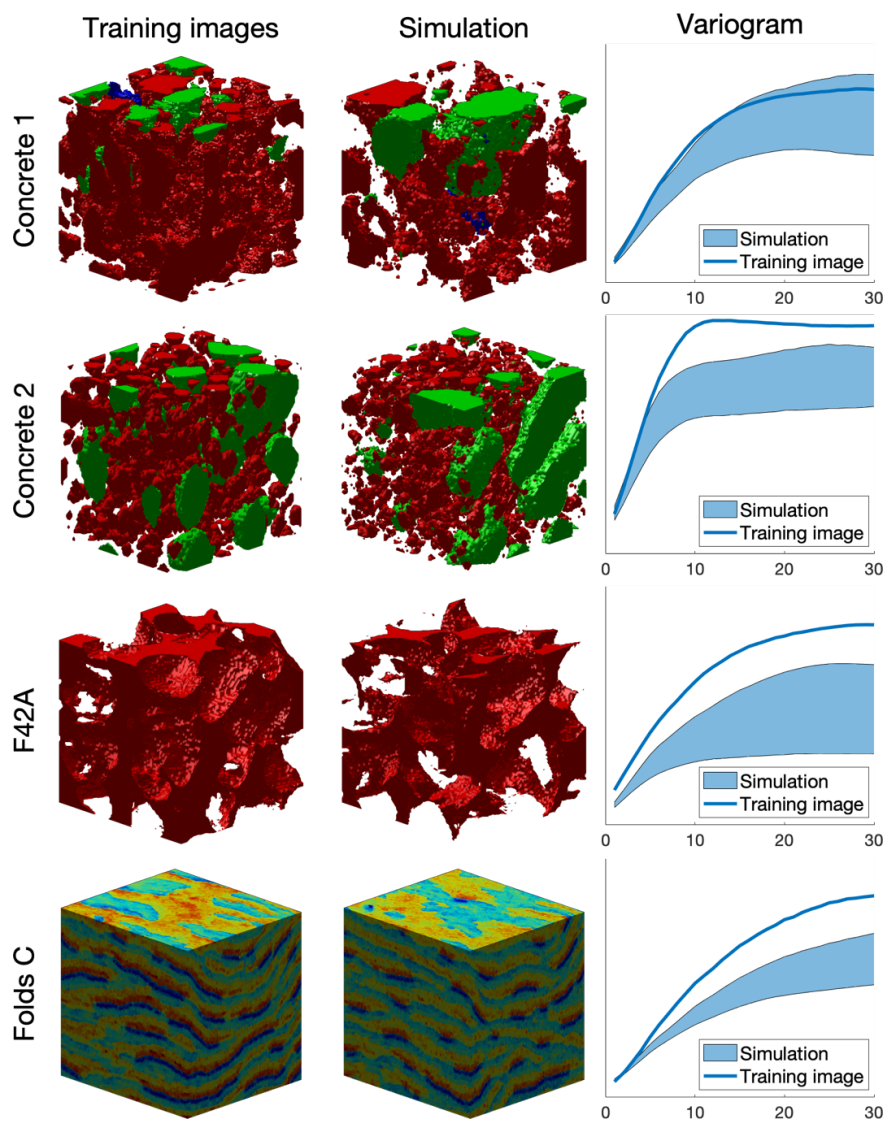
619 *Figure A 2 Examples of 2D simulations: the first 3 rows represent 3 variables of a single*
 620 *simulation*
 621

622



623

624



625

626

Figure A 3 Examples of 3D simulation results



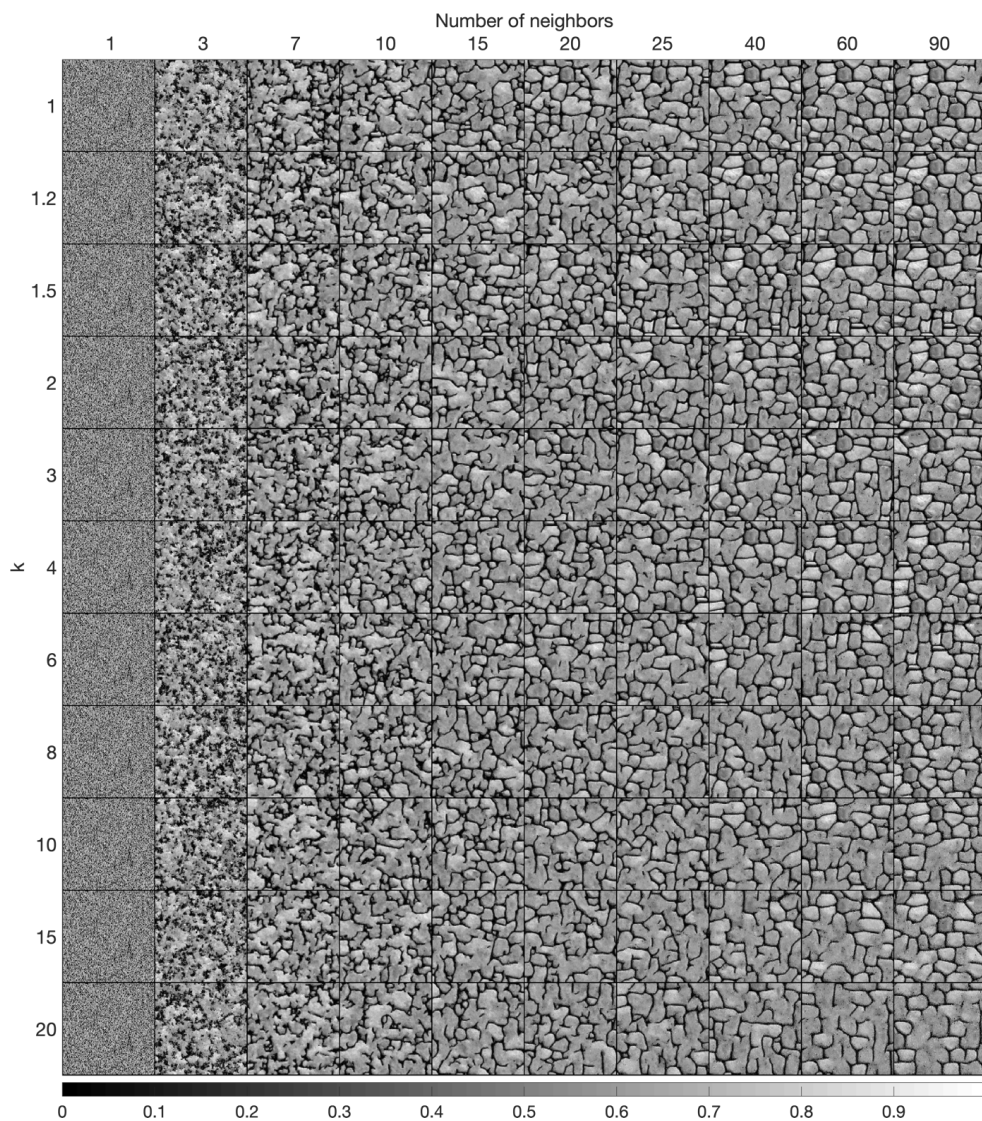
	Herten	Stone
Source	(Mariethoz and Caers, 2014)	(Mariethoz and Caers, 2014)
Size of the training image (px)	716 × 350	200 × 200
Size of the Simulation (px)	716 × 350	200 × 200
Computation time (s)	1133	21
k	1.2	
N	80	

627 *Table A 3 Simulation parameters for Figure A 2. Times are specified for simulations without*
 628 *parallelization.*

629

	Concrete 1	Concrete 2	F42A	Folds continues
Source	(Meerschman et al., 2013)	(Meerschman et al., 2013)	Doi:10.6084/m9.figshare.1189259	(Mariethoz and Caers, 2014)
Size of the training image (px)	150 × 150 × 150	100 × 90 × 80	100 × 100 × 100	180 × 150 × 120
Size of the simulation (px)	100 × 100 × 100	100 × 100 × 100	100 × 100 × 100	180 × 150 × 120
Computation time (s)	11436	1416	1638	7637
k	1.2			
N	50		125	

630 *Table A 4 Simulation parameters for Figure A 3. Times are specified for simulations without*
 631 *parallelization.*



632

633

634

Figure A 4 Complete sensitivity analysis, with one simulation for the two main parameters of QS

635

636

637

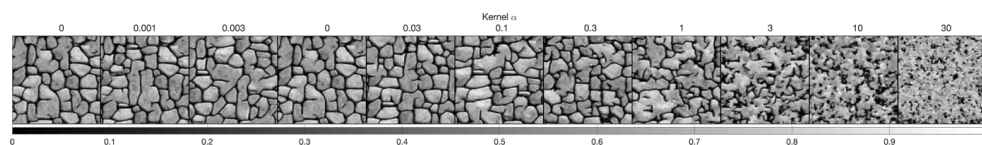


Figure A 5 Complete sensitivity analysis, with one simulation for each kernel with $k=1.5$ and $N=40$



638 **9. Acknowledgments**

639 This research was funded by the Swiss National Science Foundation, grant number
640 200021_162882. Thanks to Intel for allowing us to conduct numerical experiments on their
641 latest hardware using the AI DevCloud. Thanks to Luiz Gustavo Rasera for his comments,
642 which greatly improved the manuscript; to Ehsan Baninajar for running his optimization
643 method, which improved the reliability of the benchmarks; and to all the early users of QS for
644 their useful feedback and their patience in waiting for this manuscript.

645

646

647 **10. References**

- 648 Arpat, G. B. and Caers, J.: Conditional Simulation with Patterns, *Mathematical Geology*,
649 39(2), 177–203, doi:10.1007/s11004-006-9075-3, 2007.
- 650 Bancheri, M., Serafin, F., Bottazzi, M., Abera, W., Formetta, G. and Rigon, R.: The design,
651 deployment, and testing of kriging models in GEOframe with SIK-0.9.8, *Geosci. Model Dev.*,
652 11(6), 2189–2207, doi:10.5194/gmd-11-2189-2018, 2018.
- 653 Baninajar, E., Sharghi, Y. & Mariethoz, G.: MPS-APO: a rapid and automatic parameter
654 optimizer for multiple-point geostatistics, *Stoch Environ Res Risk Assess*, 33: 1969–1989,
655 doi:10.1007/s00477-019-01742-7, 2019
- 656 Barfod, A. A. S., Vilhelmsen, T. N., Jørgensen, F., Christiansen, A. V., Høyer, A.-S.,
657 Straubhaar, J. and Møller, I.: Contributions to uncertainty related to hydrostratigraphic
658 modeling using multiple-point statistics, *Hydrol. Earth Syst. Sci.*, 22(10), 5485–5508,
659 doi:10.5194/hess-22-5485-2018, 2018.
- 660 Cooley, J. W., computation, J. T. M. O.1965: An algorithm for the machine calculation of
661 complex Fourier series, *JSTOR*, 19(90), 297, doi:10.2307/2003354, 1965.
- 662 Dong, H. and Blunt, M. J.: Pore-network extraction from micro-computerized-tomography
663 images, *Phys. Rev. E*, 80(3), 84–11, doi:10.1103/PhysRevE.80.036307, 2009.
- 664 Frigo, M. and Johnson, S. G.: FFTW, [online] Available from: <http://www.fftw.org/fftw3.pdf>,
665 2018.
- 666 Gauss, C. F.: *Demonstratio nova theorematis omnem functionem algebraicam*. 1799.
- 667 Gómez-Hernández, J. J. and Journel, A. G.: Joint Sequential Simulation of MultiGaussian
668 Fields, in *Geostatistics Tróia '92*, vol. 5, pp. 85–94, Springer, Dordrecht, Dordrecht. 1993.
- 669 Graeler, B., Pebesma, E. and Heuvelink, G.: Spatio-Temporal Interpolation using gstat, *R*
670 *Journal*, 8(1), 204–218, 2016.



- 671 Gravey, M., Rasera, L. G. and Mariethoz, G.: Analogue-based colorization of remote sensing
672 images using textural information, *ISPRS Journal of Photogrammetry and Remote Sensing*,
673 147, 242–254, doi:10.1016/j.isprsjprs.2018.11.003, 2019.
- 674 Guardiano, F. B. and Srivastava, R. M.: Multivariate Geostatistics: Beyond Bivariate
675 Moments, in *Geostatistics Tróia '92*, vol. 5, pp. 133–144, Springer, Dordrecht, Dordrecht.
676 1993.
- 677 Hamming, R. W.: Error detecting and error correcting codes, edited by The Bell system
678 technical, *The Bell system technical*, 29(2), 147–160, doi:10.1002/j.1538-
679 7305.1950.tb00463.x, 1950.
- 680 Hoffmann, J., Scheidt, C., Barfod, A., Caers, J.: 2017: Stochastic simulation by image quilting
681 of process-based geological models, Elsevier, doi:10.1016/j.cageo.2017.05.012, 2017.
- 682 Honarkhah, M. and Caers, J.: Stochastic Simulation of Patterns Using Distance-Based Pattern
683 Modeling, *Math Geosci*, 42(5), 487–517, doi:10.1007/s11004-010-9276-7, 2010.
- 684 Intel Corporation: Intel® Math Kernel Library Reference Manual - C, 1–2606, 2019.
- 685 Jha, S. K., Mariethoz, G., Evans, J., McCabe, M. F. and Sharma, A.: A space and time scale-
686 dependent nonlinear geostatistical approach for downscaling daily precipitation and
687 temperature, *Water Resources Research*, 51(8), 6244–6261, doi:10.1002/2014WR016729,
688 2015.
- 689 John Paul Shen, M. H. L.: *Modern Processor Design: Fundamentals of Superscalar*
690 *Processors*, 1–658, 2018.
- 691 Latombe, G., Burke, A., Vrac, M., Levavasseur, G., Dumas, C., Kageyama, M. and Ramstein,
692 G.: Comparison of spatial downscaling methods of general circulation model results to study
693 climate variability during the Last Glacial Maximum, *Geosci. Model Dev.*, 11(7), 2563–2579,
694 doi:10.5194/gmd-11-2563-2018, 2018.
- 695 Li, J. and Heap, A. D.: Spatial interpolation methods applied in the environmental sciences: A
696 review, *Environ Model Softw*, 53(C), 173–189, doi:10.1016/j.envsoft.2013.12.008, 2014.
- 697 Li, X., Mariethoz, G., Lu, D. and Linde, N.: Patch-based iterative conditional geostatistical
698 simulation using graph cuts, *Water Resources Research*, 52(8), 6297–6320,
699 doi:10.1002/2015WR018378, 2016.
- 700 Mahmud, K., Mariethoz, G., Caers, J., Tahmasebi, P. and Baker, A.: Simulation of Earth
701 textures by conditional image quilting, *Water Resources Research*, 50(4), 3088–3107,
702 doi:10.1002/2013WR015069, 2014.
- 703 Mariethoz, G.: A general parallelization strategy for random path based geostatistical
704 simulation methods, *Computers and Geosciences*, 36(7), 953–958,
705 doi:10.1016/j.cageo.2009.11.001, 2010.
- 706 Mariethoz, G. and Caers, J.: *Multiple-point geostatistics: stochastic modeling with training*
707 *images*, Wiley. 2014.



- 708 Mariethoz, G. and Kelly, B. F. J.: Modeling complex geological structures with elementary
709 training images and transform-invariant distances, *Water Resources Research*, 47(7), 959–14,
710 doi:10.1029/2011WR010412, 2011.
- 711 Mariethoz, G. and Lefebvre, S.: Bridges between multiple-point geostatistics and texture
712 synthesis_ Review and guidelines for future research, *Computers and Geosciences*, 66(C),
713 66–80, doi:10.1016/j.cageo.2014.01.001, 2014.
- 714 Mariethoz, G., Renard, P. and Straubhaar, J.: The Direct Sampling method to perform
715 multiple-point geostatistical simulations, *Water Resources Research*, 46(11),
716 doi:10.1029/2008WR007621, 2010.
- 717 Matheron, G.: The intrinsic random functions and their applications, *Advances in Applied*
718 *Probability*, 5(3), 439–468, doi:10.2307/1425829, 1973.
- 719 Meerschman, E., Pirot, G., Mariethoz, G., Straubhaar, J., Van Meirvenne, M. and Renard, P.:
720 A practical guide to performing multiple-point statistical simulations with the Direct
721 Sampling algorithm, *Computers and Geosciences*, 52(C), 307–324,
722 doi:10.1016/j.cageo.2012.09.019, 2013.
- 723 Oriani, F., Ohana-Levi, N., Marra, F., Straubhaar, J., Mariethoz, G., Renard, P., Karnieli, A.
724 and Morin, E.: Simulating Small-Scale Rainfall Fields Conditioned by Weather State and
725 Elevation: A Data-Driven Approach Based on Rainfall Radar Images, *Water Resources*
726 *Research*, 15(4), 265, doi:10.1002/2017WR020876, 2017.
- 727 Rasera L.G., Gravey M., Lane S. N., Mariethoz G. Downscaling images with trends using
728 multiple-point statistics simulation: An application to digital elevation models, *Mathematical*
729 *Geosciences*, 1– 43, doi:10.1007/s11004-019-09818-4, 2019
- 730 Renard, P. and Allard, D.: Connectivity metrics for subsurface flow and transport, *Advances*
731 *in Water Resources*, 51(C), 168–196, doi:10.1016/j.advwatres.2011.12.001, 2013.
- 732 Rodríguez, P.: A radix-2 FFT algorithm for modern single instruction multiple data (SIMD)
733 architectures, doi:10.1109/ICASSP.2002.5745335, 2002.
- 734 Shannon: A mathematical theory of communication, Wiley Online Library, 1948.
- 735 Straubhaar, J., Renard, P., Mariethoz, G., Froidevaux, R. and Besson, O.: An Improved
736 Parallel Multiple-point Algorithm Using a List Approach, *Math Geosci*, 43(3), 305–328,
737 doi:10.1007/s11004-011-9328-7, 2011.
- 738 Strebelle, S.: Conditional simulation of complex geological structures using multiple-point
739 statistics, *Mathematical Geology*, 34(1), 1–21, doi:10.1023/A:1014009426274, 2002.
- 740 Strebelle, S., Payrazyan, K. and Caers, J.: Modeling of a Deepwater Turbidite Reservoir
741 Conditional to Seismic Data Using Multiple-Point Geostatistics, *Society of Petroleum*
742 *Engineers*. 2002.
- 743 Tadić, J. M., Qiu, X., Miller, S. and Michalak, A. M.: Spatio-temporal approach to moving
744 window block kriging of satellite data v1.0, *Geosci. Model Dev.*, 10(2), 709–720,
745 doi:10.5194/gmd-10-709-2017, 2017.



- 746 Tadić, J. M., Qiu, X., Yadav, V. and Michalak, A. M.: Mapping of satellite Earth observations
747 using moving window block kriging, *Geosci. Model Dev.*, 8(10), 3311–3319,
748 doi:10.5194/gmd-8-3311-2015, 2015.
- 749 Tahmasebi, P.: Structural Adjustment for Accurate Conditioning in Large-Scale Subsurface
750 Systems, *Advances in Water Resources*, 1–52, doi:10.1016/j.advwatres.2017.01.009, 2017.
- 751 Tahmasebi, P., Sahimi, M., Mariethoz, G. and Hezarkhani, A.: Accelerating geostatistical
752 simulations using graphics processing units (GPU), *Computers and Geosciences*, 46(C), 51–
753 59, doi:10.1016/j.cageo.2012.03.028, 2012.
- 754 Vannamettee, E., Babel, L. V., Hendriks, M. R., Schuur J.: Semi-automated mapping of
755 landforms using multiple point geostatistics, *Elsevier*, doi:10.1016/j.geomorph.2014.05.032,
756 2014.
- 757 Wojcik, R., McLaughlin, D., on, A. K. I. T.2009: Conditioning stochastic rainfall replicates
758 on remote sensing data, doi:10.1109/TGRS.2009.2016413, 2009.
- 759 Yin, G., Mariethoz, G. and McCabe, M.: Gap-Filling of Landsat 7 Imagery Using the Direct
760 Sampling Method, *Remote Sensing*, 9(1), 12, doi:10.3390/rs9010012, 2017.